Adaptive Delay Compensator Based Model Predictive Control for Paralleled VSG-SG System in Islanded Microgrids

Mohammadreza Najafi, Hossein Aliamooei-Lakeh, Hessam Kazari, and Mohammadreza Toulabi

***Abstract*—The increasing integration of inverter-based renewable energy sources (RESs) has significantly reduced the power grid inertia, leading to challenges in maintaining frequency stability. Virtual synchronous generators (VSGs), which emulate the behavior of synchronous generators (SGs), can help address this issue by providing synthetic inertia and improving system stability during disturbances. The paralleled operation of VSGs and SGs is particularly important in islanded microgrids, where small SGs are commonly used for power generation. This paper presents a comprehensive dynamic model of a paralleled VSG-SG system and proposes a model predictive control (MPC) strategy for VSG to enhance disturbance rejection and improve dynamic performance. Additionally, an adaptive delay compensator (ADC) is introduced to manage communication delays between the control center and system. Simulation results in MATLAB/Simulink demonstrate the effectiveness of the MPC-based VSG control method in improving frequency control in various disturbance scenarios.**

***Index Terms*—Frequency control, microgrid (MG), model predictive control (MPC), delay compensator, virtual synchronous generator (VSG), synchronous generator (SG), renewable energy source (RES), inertia.**

NOMENCLATURE

A. Variable

τ_d	Amount of delay
θ_{SG}	Phase angle difference between synchronous generator (SG) and reference frame
δ_{SG}, δ_{VSG}	Phase angles of SG and virtual synchronous generator (VSG)
ω_{SG}, ω_{VSG}	Angular frequencies of SG and VSG
ω_0	Frequency reference
$\boldsymbol{\omega}(t)$	Reference signal
d, q	Indices of d- and q-axis variables
D_{SG}	Damping coefficient of SG
D_1	Damping coefficient of VSG
E_{SG}	Electromotive force of SG
E_1	Electromotive force of VSG
E_f	Field excitation of SG
F	Electrical quantity like voltage and current
i_{SG}	Current of SG line
i_1	Current of VSG line
K_{P1}, K_{P2}	Proportional coefficients in proportional-integral (PI) controller
K_{I1}, K_{I2}	Integral coefficients in PI controller
$K_{p_{SG}}$	Active droop coefficient of SG
K_{p_1}	Active droop coefficient of VSG
K_{q_1}	Reactive droop coefficient of VSG
K_1	Integral controller coefficient of VSG
M_{SG}	Inertia constant of SG
M_1	Inertia constant of VSG
N_c	Control horizon
N_p	Predicted horizon
n	A positive integer
P_e	Electrical output power of SG
P_m	Mechanical input power of SG
$P_{0_{SG}}$, P_{0_1}	Reference active power of SG and VSG
P_{in_1}	Input active power of VSG
P_{out_1}, Q_{out_1}	Output active power and reactive power of VSG
Q_{0_1}	Reference reactive power of VSG
R_1, L_1	Resistance and inductance of VSG line
R_x, L_x	Resistance and inductance of SG line
R_v, L_v	Virtual resistance and inductance of VSG
R_f, L_f, C_f	Resistance, inductance, and capacitance of RLC filter for VSG
R_L, L_L	Resistance and inductance of RL load
S_{base}, v_{base}	Base capacity and voltage
$T_{d_{SG}}$	Governor delay of SG
$T_{0_{SG}}$	Open-circuit time constant of SG

Manuscript received: November 22, 2024; revised: April 27, 2025; accepted: July 3, 2025. Date of CrossCheck: July 3, 2025. Date of online publication: August 25, 2025.

M. Najafi, H. Aliamoooei-Lakeh, and M. Toulabi are with the Department of Electrical Engineering, K. N. Toosi University of Technology, Tehran, Iran (e-mail: mohamadreza.najafi@email.kntu.ac.ir; babak.amoo2000@email.kntu.ac.ir; toulabi@kntu.ac.ir).

H. Kazari (corresponding author) is with the Department of Electrical Engineering, Iran University of Science and Technology, Tehran, Iran (e-mail: hkazari@iust.ac.ir).

DOI: 10.35833/MPCE.2024.001254

T_{d_1}	Governor delay of VSG
T_c	Time constant
V_o, i_o	Output voltage and current of VSG
V_b	Voltage of node *b*
V_1	Voltage of arbitrary node connected with VSG
W_i	Weighting factor
X_{SG}	Reactance of SG
X'_{SG}	Transient reactance of SG

B. Matrix and Vector

$\boldsymbol{A}$, $\boldsymbol{B}$, $\boldsymbol{Y}$	State, input, and output matrices
$\boldsymbol{I}$	Identity matrix
$\tilde{\boldsymbol{u}}$	Predicted optimal control input vector over a finite future horizon
$\boldsymbol{x}$	State vector
$\tilde{\boldsymbol{y}}$	Predicted output vector

I. Introduction

CLIMATE change and excessive consumption of fossil fuels have led to the widespread development of distributed generators (DGs) and renewable energy sources (RESs) such as solar, wind, hydro, and biofuels [1]. These advancements are primarily driven by the need to reduce greenhouse gas emissions and mitigate air pollution [2]. In microgrid applications, inverters serve as vital power electronic interfaces, enabling the integration of DGs into the power system [3], [4]. However, compared with traditional synchronous generators (SGs), power grids dominated by inverter-based RESs suffer from significantly reduced inertia and damping characteristics [5], [6]. This reduction in inertia, particularly with the high penetration of RESs, can lead to frequency deviations and instability under disturbances [7].

Control strategies based on virtual synchronous generators (VSGs) have been proposed to overcome these challenges. VSGs emulate the electromechanical behavior of traditional SGs using advanced control algorithms and power electronic interfaces. This emulation allows them to provide synthetic inertia and damping, improving the frequency response and dynamic stability of system. VSGs achieve this by emulating the frequency and voltage control characteristics of synchronous machines, either fully or partially, depending on the configuration of grid-connected converters [8]-[11]. Various VSG topologies and structures have been discussed in [12].

VSGs offer significant advantages over physical SGs, primarily through tunable parameters that enhance the system dynamic response and adaptability [13]-[15]. Recent research has explored various control strategies to optimize the VSG performance, addressing the limitations of traditional and advanced control strategies. Although the proportional-integral-derivative (PID) controllers remain widely used, their performance degrades under disturbances [16]. To overcome this problem, adaptive strategies have been proposed, such as a self-adjusting scheme for real-time active power regulation [17] and an optimal frequency control method using adaptive dynamic programming for virtual inertia tuning [18]. Data-driven approaches such as an optimal inertia controller that adapts to system dynamics [19] and adaptive fuzzy neural network-based decoupling strategies [20] improve the robustness at the cost of increased complexity. Similarly, the H_∞ control methods enhance active power regulation but introduce trade-offs in overshoot and settling time compared with droop control [21]. To mitigate the frequency deviations under disturbances, fuzzy logic controllers with virtual inertia have been introduced [22], [23]. Additionally, the robust control designs for extended VSGs [24] and state-feedback controllers [10], ensuring dynamic stable operation in both grid-connected and islanded modes, have been investigated, further advancing VSG reliability.

Model predictive control (MPC), which is an optimization-based control strategy, has recently gained significant attention owing to its ability to predict system behavior and compute control actions accordingly. MPC handles system constraints, manages multi-input multi-output (MIMO) nonlinear dynamics, and offers robust performance under uncertainties. MPC provides superior transient responses and disturbance rejections compared with traditional control methods such as PID and fuzzy logic. For example, [25] proposes a double-loop cascaded MPC structure to improve frequency regulation in islanded microgrids with multiple VSGs. This control shows reduced settling time and lower frequency deviation. Likewise, [26] introduces a fractional-order VSG controller using MPC, demonstrating improved frequency nadir recovery and smoother dynamics than conventional methods. Unlike conventional feedback-based methods, MPC incorporates predictive capabilities, enabling the anticipation of disturbances and appropriate action planning. In [27], an MPC-based VSG framework is introduced for islanded microgrids using energy storage systems, where the real-time frequency detection is used to forecast the optimal power output. A cascaded MPC structure is proposed in [25], allowing flexible control objectives to be achieved with vector selection and minimizing the tracking error. In [26], a VSG-MPC controller is presented to reduce the system order and mitigate active power fluctuations. However, a critical challenge in applying MPC to frequency regulation lies in the presence of communication delays. As discussed in [28], such delays can arise from the type of communication medium, physical distance, or network load. If not considered, these delays can degrade the control performance and even destabilize the system, particularly in real-time control applications where feedback from a centralized controller is involved.

Islanded microgrids typically consist of DGs and one or more backup SGs (e.g., diesel or gas SGs). As the paralleled operation of VSGs and SGs becomes increasingly common, the development of robust control strategies that explicitly account for delay is essential particularly in isolated systems. Several studies have addressed the modeling of paralleled VSG-SG systems. In [29], a small-signal model of VSG with governor dynamics is developed, producing a two-zone system combining SGs and VSGs. The influence of VSGs on damping low-frequency oscillations in the power grid is compared with that of SGs. In [30], the damping characteristics of a paralleled VSG-SG system are analyzed through transient energy methods. However, these studies pri-

marily offer experimental validation and lack a comprehensive theoretical model. Moreover, they often ignore the effects of frequency regulation and rely on simplified assumptions such as purely resistive loads, whereas, in real systems, load impedances are complex.

Although a wide range of studies have explored VSG-MPC systems for frequency regulation in islanded microgrids, several significant knowledge gaps remain. First, most studies neglect the influence of communication delays, which are inherent in real-time control environments. These delays caused by data transmission between the controller and physical units can significantly impair the effectiveness of MPC and potentially lead to instability. For instance, the MPC approaches in [18], [25], and [27] assume ideal communication links and fail to account for the practical impact of data latency. Second, the integrated modeling frameworks that simultaneously consider the physical characteristics of both SGs and VSGs under non-ideal communication conditions are scarce. Finally, although the simulation-based evaluations are common, very few studies have proposed adaptive delay mitigation techniques or compensators tailored for real-time VSG-MPC applications. To address these limitations, this study develops a comprehensive dynamic model for a paralleled VSG-SG system in an islanded microgrid, explicitly accounting for communication delays. An adaptive delay compensator (ADC) is incorporated into the MPC framework to mitigate the impact of latency. The MPC-based VSG control method enhances system stability and improves frequency control performance without increasing the complexity of implementation, which makes it not only theoretically sound but also practically applicable in real-world microgrids. The key contributions of this paper are as follows.

1) Development of a detailed dynamic model for paralleled VSG-SG system that accounts for all relevant electrical and control constraints.

2) Proposal of an MPC-based VSG control method for frequency regulation that improves the dynamic response of both the VSG and SG under various disturbances.

3) Introduction of an ADC integrated into the control framework to counteract communication delays in real-time frequency control.

4) Extensive simulations in MATLAB/Simulink demonstrating the effectiveness of the MPC-based VSG control method in different disturbance and delay scenarios.

The remainder of this paper is organized as follows. Section II introduces the paralleled operation of VSG and SG. Section III introduces the MPC-based VSG controller for frequency regulation. In Section IV, the effectiveness of the MPC-based VSG control method is evaluated through simulations under various disturbance and delay conditions. Finally, Section V concludes this paper.

II. Paralleled Operation of VSG and SG

In this section, first, the dynamic model of SG is introduced. Then, the dynamic model of VSG is developed using the same approach. Finally, the paralleled operation of VSG and SG is explained.

A. Dynamic Model of SG

In this paper, to make a balance between the computational efficiency and accuracy in capturing the key dynamics of system, we employ the fifth-order SG model for system simulations. The fifth-order SG model is commonly used in similar studies and provides a reasonable approximation of the dynamic behavior of SG, capturing essential features such as rotor dynamics, excitation system, and governor dynamics. It is chosen for its ability to model the most critical aspects of the system without introducing unnecessary complexity. In terms of impact, the simplification to a fifth-order SG model does not significantly affect the overall analysis of the dynamic performance for the specific focus of this paper, which is on frequency regulation in a microgrid context. Higher-order models could potentially offer more detailed representation; however, the additional complexity would increase the computational burden and may not lead to significantly different results within the scope of the analysis performed in this paper. The mathematical representation of this dynamic fifth-order SG model typically takes the following form [31], [32]:

$$\begin{cases} \dot{\delta}_{SG} = \omega_0 \omega_{SG} \\ \dot{\omega}_{SG} = -\dfrac{D_{SG}}{M_{SG}}(\omega_{SG} - \omega_0) + \dfrac{1}{M_{SG}}(P_m - P_e) \\ \dot{E}_{SG_d} = \dfrac{1}{T_{0_{SGq}}}[-E_{SG_d} + (X_{SG_q} - X'_{SG_q}) i_{SG_q}] \\ \dot{E}_{SG_q} = \dfrac{1}{T_{0_{SGd}}}[-E_{SG_q} + E_f + (X_{SG_d} - X'_{SG_d}) i_{SG_d}] \\ \dot{P}_m = \dfrac{1}{T_{d_{SG}}}[-K_{SG}(\omega_{SG} - \omega_0) - P_m + P_{0_{SG}}] \end{cases} \tag{1}$$

The d- and q-axis terminal voltages of SG line are formulated as:

$$\begin{cases} V_{SG_d} = E_{SG_d} - X'_{SG_q} i_{SG_q} \\ V_{SG_q} = E_{SG_q} - X'_{SG_d} i_{SG_d} \end{cases} \tag{2}$$

Additionally, the electrical output power of SG is expressed as:

$$P_e = V_{SG_d} i_{SG_d} + V_{SG_q} i_{SG_q} \tag{3}$$

The nonlinear model of SG can then be built using (1)-(3).

B. Dynamic Model of VSG

As depicted in Fig. 1, the VSG operates as an interface between all types of energy storage units, generation units, and power grid. An inverter with current control is the foundation of the VSG control. A vital component of the VSG is the swing equation like SG [10], as illustrated by the stucture of VSG control strategy shown in Fig. 2. The swing equation of VSG is represented as:

$$\dot{\omega}_{VSG} = -\frac{D_1}{M_1}(\omega_{VSG} - \omega_0) + \frac{1}{M_1}(P_{in_1} - P_{out_1}) \tag{4}$$

It should be noted that the governor model uses the frequency-active power droop characteristic to generate the input active power of VSG. The dynamic equation for the input active power of VSG is expressed as:

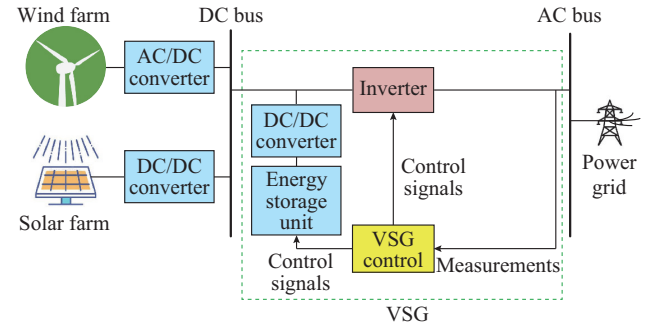

Fig. 1. Conceptual structure of VSG.

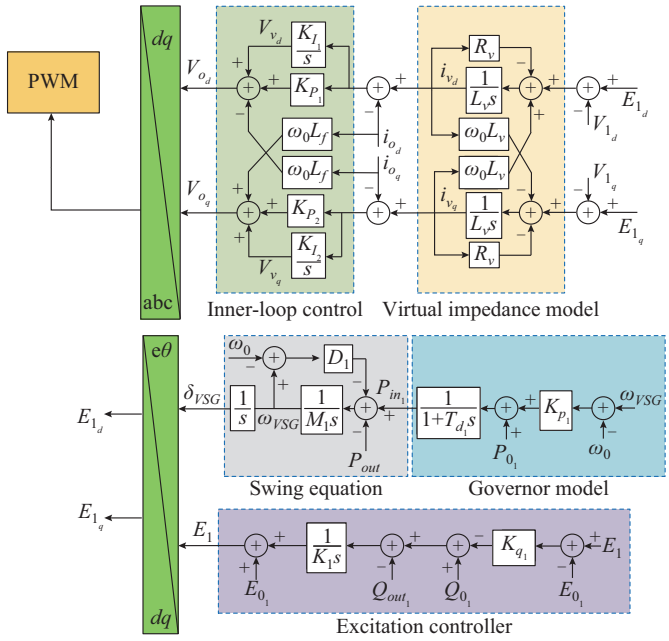

Fig. 2. Structure of VSG control strategy.

$$\dot{P}_{in_1} = \frac{1}{T_{d_1}}\left[-K_{p_1}(\omega_{VSG}-\omega_0) - P_{in_1} + P_{0_1}\right] \tag{5}$$

The excitation controller mimics the automated voltage regulator and demonstrates the field winding characteristics of SG. The voltage-reactive power droop characteristic and an integral controller are used to control the reactive power of the VSG. The state equation of VSG is expressed as:

$$\dot{E}_1 = \frac{-K_{q_1}}{K_1}(E_1 - E_{0_1}) + \frac{1}{K_1}(Q_{0_1} - Q_{out_1}) \tag{6}$$

By making the q axis paralleled to the direction of E_1, the d- and q-axis electromotive forces of VSG are expressed as:

$$\begin{cases} E_{1_d} = 0 \\ E_{1_q} = E_1 \end{cases} \tag{7}$$

In addition, using (7) and the output voltage of VSG, it is possible to obtain the d- and q-axis output currents of virtual impedance, whose state equations are expressed as:

$$\begin{cases} \dot{i}_{v_d} = \dfrac{E_{1_d} - V_{1_d} - R_v i_{v_d} + \omega_0 L_v i_{v_q}}{L_v} \\ \dot{i}_{v_q} = \dfrac{E_{1_q} - V_{1_q} - R_v i_{v_q} - \omega_0 L_v i_{v_d}}{L_v} \end{cases} \tag{8}$$

As illustrated in Fig. 2, the state equations of the d- and q-axis output voltages of virtual impedance are given by:

$$\begin{cases} \dot{V}_{v_d} = K_{I_1}(i_{v_d} - i_{o_d}) \\ \dot{V}_{v_q} = K_{I_2}(i_{v_q} - i_{o_q}) \end{cases} \tag{9}$$

$$\begin{cases} V_{o_d} = V_{v_d} + K_{P_1}(i_{v_d} - i_{o_d}) - \omega_0 L_f i_{o_q} \\ V_{o_q} = V_{v_q} + K_{P_2}(i_{v_q} - i_{o_q}) + \omega_0 L_f i_{o_d} \end{cases} \tag{10}$$

The output active power and reactive power of VSG are determined using the output voltage and current of VSG as:

$$\begin{cases} P_{out_1} = V_{o_d} i_{o_d} + V_{o_q} i_{o_q} \\ Q_{out_1} = V_{o_d} i_{o_q} - V_{o_q} i_{o_d} \end{cases} \tag{11}$$

It should be noted that the oscillation in low-frequency experiments is significantly slower than the inverter dynamics. Therefore, ignoring the inverter dynamics has no impact on the correctness of the model [10]. Consequently, the inverter dynamics are not considered in this paper.

C. Paralleled Operation of VSG and SG

The equivalent circuit of the paralleled VSG-SG system, which consists of VSG, SG, RLC filter, lines, and RL load, is shown in Fig. 3. Through an RLC filter, each VSG is linked to an arbitrary node i. A shunt capacitor and series RL branch construct the RLC filter. The state equations for the d- and q-axis output currents of VSG are expressed as:

$$\begin{cases} \dot{i}_{o_d} = \dfrac{1}{L_f}(V_{o_d} - V_{1_d} - R_f i_{o_d} + \omega_0 L_f i_{o_q}) \\ \dot{i}_{o_q} = \dfrac{1}{L_f}(V_{o_q} - V_{1_q} - R_f i_{o_q} - \omega_0 L_f i_{o_d}) \end{cases} \tag{12}$$

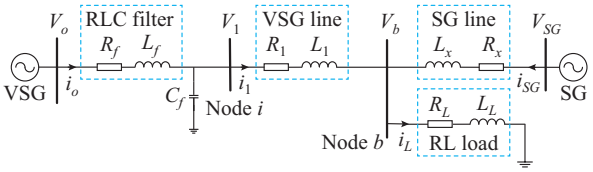

Fig. 3. Equivalent circuit of paralleled VSG-SG system.

Besides, the d- and q-axis voltages of node i are expressed as:

$$\begin{cases} \dot{V}_{1_d} = \dfrac{1}{C_f}(i_{o_d} - i_{1_d} + \omega_0 C_f V_{1_q}) \\ \dot{V}_{1_q} = \dfrac{1}{C_f}(i_{o_q} - i_{1_q} - \omega_0 C_f V_{1_d}) \end{cases} \tag{13}$$

To obtain the system model using the transformation equations (14) and (15), the voltages and currents of both the VSG and SG must be within a common reference frame. As shown in Fig. 4, dq_{VSG} is set as the common reference frame for the system, and the variables in this frame are in uppercase with subscripts D and Q.

$$\begin{bmatrix} F_D \\ F_Q \end{bmatrix} = \begin{bmatrix} \cos\theta & -\sin\theta \\ \sin\theta & \cos\theta \end{bmatrix} \begin{bmatrix} F_d \\ F_q \end{bmatrix} \tag{14}$$

$$\begin{bmatrix} F_d \\ F_q \end{bmatrix} = \begin{bmatrix} \cos\theta & \sin\theta \\ -\sin\theta & \cos\theta \end{bmatrix} \begin{bmatrix} F_D \\ F_Q \end{bmatrix} \tag{15}$$

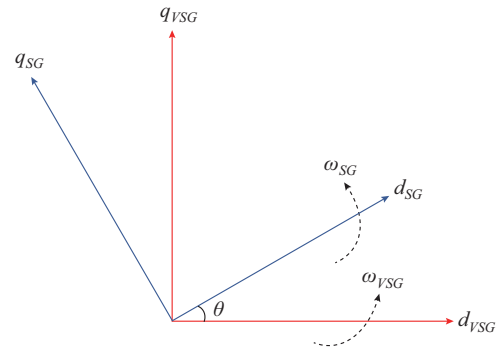

Fig. 4. Relationship between reference frame of VSG dq_{VSG} and reference frame of SG dq_{SG}.

where θ is the angle difference between dq_{VSG} and dq_{SG}, which is calculated as:

$$\begin{cases}\theta=\delta_{SG}-\delta_{VSG}\\ \dot{\theta}=\dot{\delta}_{SG}-\dot{\delta}_{VSG}=\omega_0(\omega_{SG}-\omega_{VSG})\end{cases} \tag{16}$$

For the VSG, V_1 and I_1 in the common reference frame (i.e., the D and Q axes) are produced using the transformation matrices in (14) as:

$$\begin{cases}V_{1_D}=V_{1_d}\\ V_{1_Q}=V_{1_q}\end{cases} \tag{17}$$

$$\begin{cases}I_{1_D}=i_{1_d}\\ I_{1_Q}=i_{1_q}\end{cases} \tag{18}$$

Similarly, the D- and Q-axis terminal voltages and currents of SG line are given by:

$$\begin{cases}V_{SG_D}=V_{SG_d}\cos\theta-V_{SG_q}\sin\theta\\ V_{SG_Q}=V_{SG_d}\sin\theta+V_{SG_q}\cos\theta\end{cases} \tag{19}$$

$$\begin{cases}I_{SG_D}=i_{SG_d}\cos\theta-i_{SG_q}\sin\theta\\ I_{SG_Q}=i_{SG_d}\sin\theta+i_{SG_q}\cos\theta\end{cases} \tag{20}$$

In addition, the state equations for the d- and q-axis currents of VSG line are expressed as:

$$\begin{cases}\dot{i}_{1_d}=\dfrac{1}{L_1}(V_{1_d}-V_{b_d}-R_1 i_{1_d}+\omega_0 L_1 i_{1_q})\\ \dot{i}_{1_q}=\dfrac{1}{L_1}(V_{1_q}-V_{b_q}-R_1 i_{1_q}-\omega_0 L_1 i_{1_d})\end{cases} \tag{21}$$

Similarly, the state equations for the D- and Q-axis currents of SG line are expressed as:

$$\begin{cases}\dot{I}_{SG_D}=\dfrac{1}{L_x}(V_{SG_D}-V_{b_D}-R_x I_{SG_D}+\omega_0 L_x I_{SG_Q})\\ \dot{I}_{SG_Q}=\dfrac{1}{L_x}(V_{SG_Q}-V_{b_Q}-R_x I_{SG_Q}-\omega_0 L_x I_{SG_D})\end{cases} \tag{22}$$

Furthermore, the state equations for the D- and Q-axis currents of RL load at node b are expressed as:

$$\begin{cases}\dot{I}_{L_D}=\dfrac{1}{L_L}(V_{b_D}-R_L I_{L_D}+\omega_0 L_L I_{L_Q})\\ \dot{I}_{L_Q}=\dfrac{1}{L_L}(V_{b_Q}-R_L I_{L_Q}-\omega_0 L_L I_{L_D})\end{cases} \tag{23}$$

The following equations are obtained using Kirchhoff's current law (KCL) at node b in Fig. 3 as:

$$\begin{cases}I_{L_D}=I_{1_D}+I_{SG_D}\\ I_{L_Q}=I_{1_Q}+I_{SG_Q}\end{cases} \tag{24}$$

By differentiating (24), we have:

$$\begin{cases}\dot{I}_{L_D}=\dot{I}_{1_D}+\dot{I}_{SG_D}\\ \dot{I}_{L_Q}=\dot{I}_{1_Q}+\dot{I}_{SG_Q}\end{cases} \tag{25}$$

Equation (23) can be rewritten based on (24) and (25) as:

$$\begin{cases}\dot{I}_{1_D}+\dot{I}_{SG_D}=\dfrac{1}{L_L}[V_{b_D}-R_L(I_{1_D}+I_{SG_D})+\omega_0 L_L(I_{1_Q}+I_{SG_Q})]\\ \dot{I}_{1_Q}+\dot{I}_{SG_Q}=\dfrac{1}{L_L}[V_{b_Q}-R_L(I_{1_Q}+I_{SG_Q})-\omega_0 L_L(I_{1_D}+I_{SG_D})]\end{cases} \tag{26}$$

By substituting (21) and (22) into (26), we have:

$$\begin{cases}\dfrac{1}{L_L}[V_{b_d}-R_L(i_{1_d}+I_{SG_D})+\omega_0 L_L(i_{1_q}+I_{SG_Q})]-\dfrac{1}{L_1}(V_{1_d}-V_{b_d}-\\ \qquad R_1 i_{1_d}+\omega_0 L_1 i_{1_q})-\dfrac{1}{L_x}(V_{SG_D}-V_{b_d}-R_x I_{SG_D}+\omega_0 L_x I_{SG_Q})=0\\ \dfrac{1}{L_L}[V_{b_q}-R_L(i_{1_q}+I_{SG_Q})-\omega_0 L_L(i_{1_d}+I_{SG_D})]-\dfrac{1}{L_1}(V_{1_q}-V_{b_q}-\\ \qquad R_1 i_{1_q}-\omega_0 L_1 i_{1_d})-\dfrac{1}{L_x}(V_{SG_Q}-V_{b_q}-R_x I_{SG_Q}-\omega_0 L_x I_{SG_D})=0\end{cases} \tag{27}$$

The above system of equations must be solved to determine the voltage of node b, i.e., V_b. By utilizing V_b, the state equations for both the VSG and SG currents will be modified.

The aforementioned equations will be used to develop a nonlinear state-space model of the VSG-SG system. A linearized state-space model can be created from the nonlinear one as:

$$\begin{cases}\Delta\dot{\boldsymbol{X}}(t)=\boldsymbol{A}\Delta\boldsymbol{X}+\boldsymbol{B}\Delta\boldsymbol{U}(t)\\ \Delta\boldsymbol{Y}(t)=\boldsymbol{I}\Delta\boldsymbol{X}(t)\end{cases} \tag{28}$$

$$\begin{cases}\Delta\boldsymbol{X}=[\Delta\delta_{VSG},\Delta\omega_{VSG},\Delta E_1,\Delta V_{v_d},\Delta V_{v_q},\Delta i_{v_d},\Delta i_{v_q},\\ \qquad \Delta i_{o_d},\Delta i_{o_q},\Delta V_{1_d},\Delta V_{1_q},\Delta i_{1_d},\Delta i_{1_q},\Delta P_{in_1},\Delta\delta_{SG},\\ \qquad \Delta\omega_{SG},\Delta E_{SG_d},\Delta E_{SG_q},\Delta i_{SG_d},\Delta i_{SG_q},\Delta P_m]^{\mathrm{T}}\\ \Delta\boldsymbol{U}=[\Delta P_{0_1},\Delta Q_{0_1},\Delta P_{0_{SG}}]^{\mathrm{T}}\end{cases} \tag{29}$$

The state-space model defined in (28) represents the paralleled operation of VSG and SG linearized around the operating point.

III. MPC-BASED VSG CONTROLLER

In this section, MPC is introduced as a powerful control strategy widely used in various engineering applications. Then, an adaptive delay compensation scheme is proposed to overcome the drawbacks of communication delays.

A. MPC Theory

MPC is a control strategy that uses a mathematical model of a system to predict its future behavior and determine the

optimal control actions that will achieve the desired performance objective. At each time step, the current state of the system is measured or estimated, and an optimization problem is solved to determine the optimal control actions that will minimize a cost function or achieve a desired objective, subject to constraints on the inputs and the state of the system. The iterative approach allows the MPC to adapt to changes in the system and disturbances in real time and continually optimize the control actions to achieve the desired objective. The MPC is based on choosing the optimal input from all available input sequences in the future and focuses on specific criteria. Figure 5 demonstrates the working mechanism of the MPC. To attain the minimum error between the predicted values of states and their reference values with the least amount of control effort, the optimal control chain is employed in each step.

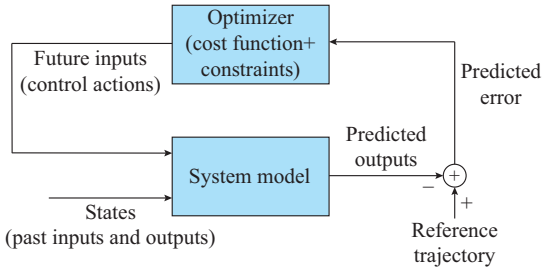

Fig. 5. Working mechanism of MPC.

The system is initially fed with the first input of the sequence using the receding horizon concept. Subsequently, the process is repeated in each sampling period, with the latest mode information incorporated. The MPC employs an iterative online optimization technique to solve a limited dynamic optimal control problem, instead of relying on the complex offline computation of the control law.

Figure 6 shows the basic structure of MPC. Based on the past, current, and desired future actions, a state-space model is used to predict the system output. The optimizer determines these actions by considering the cost function and physical and operational constraints.

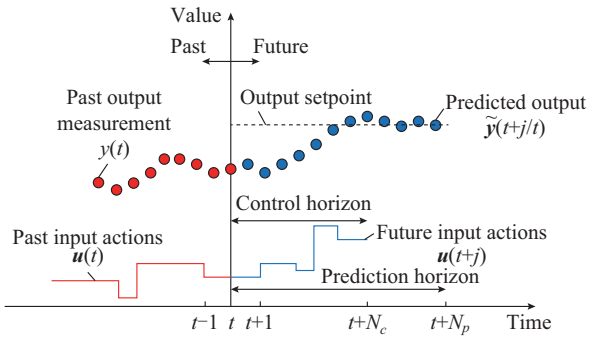

Fig. 6. Basic structure of MPC.

The following equation expresses the discrete-time state-space model of the linear system (27):

$$\begin{cases} \boldsymbol{x}(t+1)=\boldsymbol{A}\boldsymbol{x}(t)+\boldsymbol{B}\boldsymbol{u}(t) \\ \boldsymbol{y}(t)=\boldsymbol{C}\boldsymbol{x}(t) \end{cases} \tag{30}$$

According to the formula $\Delta\boldsymbol{u}(t)=\boldsymbol{u}(t)-\boldsymbol{u}(t-1)$, the model (30) can be reformulated in its augmented form to obtain offset-free control [33]:

$$\begin{cases} \begin{bmatrix} \boldsymbol{x}(t+1) \\ \boldsymbol{u}(t) \end{bmatrix} = \begin{bmatrix} \boldsymbol{A} & \boldsymbol{B} \\ \boldsymbol{0} & \boldsymbol{I} \end{bmatrix} \begin{bmatrix} \boldsymbol{x}(t) \\ \boldsymbol{u}(t-1) \end{bmatrix} + \begin{bmatrix} \boldsymbol{B} \\ \boldsymbol{I} \end{bmatrix} \Delta\boldsymbol{u}(t) \\ \boldsymbol{y}(t)=\begin{bmatrix} \boldsymbol{C} & \boldsymbol{0} \end{bmatrix} \begin{bmatrix} \boldsymbol{x}(t) \\ \boldsymbol{u}(t-1) \end{bmatrix} \end{cases} \tag{31}$$

The augmented model considering the new state vector $\tilde{\boldsymbol{x}}(t)=[\boldsymbol{x}(t) \quad \boldsymbol{u}(t-1)]^{\mathrm{T}}$ is defined as:

$$\begin{cases} \tilde{\boldsymbol{x}}(t+1)=\boldsymbol{M}\tilde{\boldsymbol{u}}(t)+\boldsymbol{N}\Delta\boldsymbol{u}(t) \\ \boldsymbol{y}(t)=\boldsymbol{Q}\tilde{\boldsymbol{x}}(t) \end{cases} \tag{32}$$

where $\boldsymbol{M}$, $\boldsymbol{N}$, and $\boldsymbol{Q}$ correspond to matrices $\boldsymbol{A}$, $\boldsymbol{B}$, and $\boldsymbol{C}$, respectively.

The cost function is used to determine the control objective and minimize the control effort while minimizing the difference between the predicted value of the system output and its reference value after the state-space model is obtained. It is worth noting that $\boldsymbol{R}$ and $\boldsymbol{P}$ are the positive definite weight matrices that are normally of diagonal form. Hence, the cost function subjected to all constraints is formulated using the following quadratic function as:

$$J(N_p,N_c)=\sum_{j=1}^{N_p}\left\| \tilde{\boldsymbol{y}}(t+j|t)-\boldsymbol{\omega}(t+j) \right\|_{\boldsymbol{R}}^2+\sum_{j=1}^{N_c}\left\| \Delta\boldsymbol{u}(t+j-1) \right\|_{\boldsymbol{P}}^2 \tag{33}$$

The optimization of the cost function in (33) is performed using quadratic programming (QP) via MATLAB solver. For real-time implementation, the QP matrices are precomputed offline, and the online optimization is executed with a short prediction horizon and warm starting to ensure fast convergence within each sampling interval. If an augmented model is employed, the output predictions to be used in the cost function (33) can be computed using (30) or (32). The predictions over the horizon are expressed as:

$$\begin{bmatrix} \tilde{\boldsymbol{y}}(t+1|t) \\ \tilde{\boldsymbol{y}}(t+2|t) \\ \vdots \\ \tilde{\boldsymbol{y}}(t+N_p|t) \end{bmatrix} = \begin{bmatrix} \boldsymbol{Q}\boldsymbol{M}\boldsymbol{x}(t)+\boldsymbol{Q}\boldsymbol{N}\Delta\boldsymbol{Q}\boldsymbol{u}(t) \\ \boldsymbol{Q}\boldsymbol{M}^2\boldsymbol{x}(t)+\sum_{i=0}^{1}\boldsymbol{Q}\boldsymbol{M}^{1-i}\boldsymbol{N}\Delta\boldsymbol{u}(t+i) \\ \vdots \\ \boldsymbol{Q}\boldsymbol{M}^{N_p}\boldsymbol{x}(t)+\sum_{i=0}^{N_p-1}\boldsymbol{Q}\boldsymbol{M}^{N_p-1-i}\boldsymbol{N}\Delta\boldsymbol{u}(t+i) \end{bmatrix} \tag{34}$$

Bold uppercase letters indicate matrices built using other matrices and vectors, whereas bold lowercase letters indicate vectors built using elements along the horizon. Note that if the state vector $\boldsymbol{x}(t)$ is not directly measurable or accessible, it can be estimated via an observer [33].

B. ADC Design

MPC relies on the communication between controllers and system components, introducing delays that can degrade performance or destabilize the system. These delays stem from the transmission of control signals between the control center and plant, whose duration is influenced by the communication medium (e.g., fiber optics, power line carriers), transmission distance, and network congestion.

To mitigate time-varying delays without excessive compu-

tational overhead, we propose an ADC based on a weighted fusion of pre-tuned compensators. By dynamically blending a small set of fixed compensators in real time, the ADC achieves a precise delay compensation while maintaining low computational complexity. This avoids the need for the online redesign of compensators and ensures rapid adaptation to varying delays. The foundation lies in the following delay representation:

$$D(s)=\mathrm{e}^{-\tau_d s}=\left(\mathrm{e}^{-\frac{\tau_d}{n}s}\right)^n=\frac{\left(\mathrm{e}^{-\frac{\tau_d}{2n}s}\right)^n}{\left(\mathrm{e}^{\frac{\tau_d}{2n}s}\right)^n}\simeq\frac{\left(1-\frac{\tau_d s}{2n}\right)^n}{\left(1+\frac{\tau_d s}{2n}\right)^n} \tag{35}$$

The ADC is used to neutralize the delay as:

$$ADC(s)=W_i(\tau_d)\frac{\left(1+\frac{T_i s}{2n}\right)^{2n}}{(1+T_c s)^{2n}}\quad i=1,2,...,m \tag{36}$$

where $T_1, T_2, ..., T_m$ are the delay values in ascending order.

The counter of each compensator is determined to compensate for part of the phase delay, and T_c depends on the system dynamics and is chosen in the range of 0.01 s to 0.1 s. $W_i(\tau_d)$ can be obtained as:

$$\begin{cases}\sum_{i=1}^{m}W_i(\tau_d)T_i^{2n}=\tau_d^{2n}\\ \sum_{i=1}^{m}W_i(\tau_d)T_i^{2n-1}=\tau_d^{2n-1}\\ \vdots\\ \sum_{i=1}^{m}W_i(\tau_d)T_i=\tau_d\\ \sum_{i=1}^{m}W_i(\tau_d)=1\end{cases} \tag{37}$$

By assuming $m=2n+1$ and using Cramer's method, $W_i(\tau_d s)$ can be uniquely obtained. A block diagram of the evolved model of the system considering ADC is shown in Fig. 7.

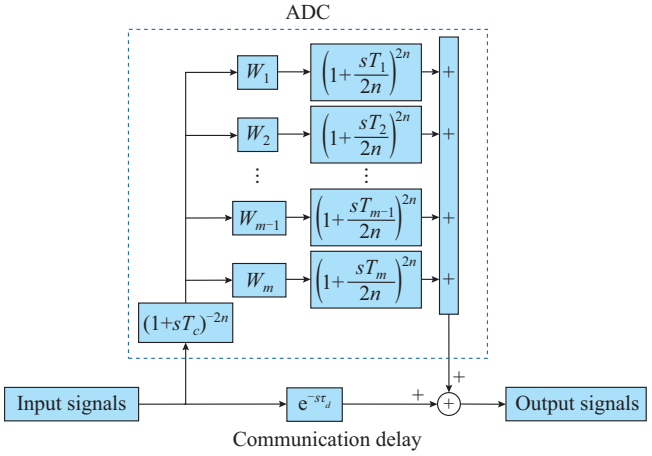

Fig. 7. Block diagram of evolved model of system considering ADC.

When $n=2$, (37) is simplified to:

$$\begin{cases}\sum_{i=1}^{5}W_i(\tau_d)T_i^4=\tau_d^4\\ \sum_{i=1}^{5}W_i(\tau_d)T_i^3=\tau_d^3\\ \sum_{i=1}^{5}W_i(\tau_d)T_i^2=\tau_d^2\\ \sum_{i=1}^{5}W_i(\tau_d)T_i^1=\tau_d\\ \sum_{i=1}^{5}W_i(\tau_d)=1\end{cases} \tag{38}$$

where T_1-T_5 are 0.1, 0.25, 0.4, 0.55, and 0.7, respectively.

IV. Simulations and Discussion

In this section, the dynamic model of the paralleled VSG-SG system is used to evaluate the effects of the MPC-based control method on the system frequency. Some disturbance scenarios listed in Table I are applied to the paralleled VSG-SG system in the simulations. As mentioned in Section III, the fifth-order SG model is considered in the simulations, and all dynamics related to the VSG, RLC filter, RL load, and lines are also considered. The specifications of the paralleled VSG-SG system are listed in Table II.

TABLE I
Disturbance Scenarios Applied to Paralleled VSG-SG System

Time (s)	ΔP_{0_1} (p.u.)	ΔQ_{0_1} (p.u.)	$\Delta P_{0_{SG}}$ (p.u.)
$0\le t<10$	0	0	0
$10\le t<25$	0.2	0	0
$25\le t<40$	0	0	0.2
$40\le t<50$	0	0.3	0

TABLE II
Specifications of Paralleled VSG-SG System

Parameter	Value	Parameter	Value	Parameter	Value
S_{base}	10 kVA	R_1	0.016 p.u.	M_1	50 s
V_{base}	200 V	L_1	0.250 p.u.	M_{SG}	30 s
ω_0	377 rad/s	R_x	0.016 p.u.	K_1	0.0125
R_L	5 p.u.	L_x	0.150 p.u.	K_{p_1}	20 p.u.
L_L	5 p.u.	X_{SG_d}	0.219 p.u.	K_{q_1}	5 p.u.
R_v	0.059 p.u.	X_{SG_q}	0.219 p.u.	$K_{p_{SG}}$	25 p.u.
L_v	0.009 p.u.	X'_{SG_d}	0.027 p.u.	N_c	2
C_f	0.600 p.u.	X'_{SG_q}	0.027 p.u.	N_p	10
R_f	0.005 p.u.	D_1	17 p.u.	τ_d	0.2 s
L_f	0.001 p.u.	D_{SG}	15 p.u.		

A. Basic VSG Control Method

This subsection discusses the operation of the paralleled VSG-SG system shown in Fig. 3 using the basic VSG control method for numerical simulations. Accordingly, the variations in the frequency and input active power of the VSG and SG with the basic VSG control method after disturbances are shown in Figs. 8(a) and 9(a), respectively.

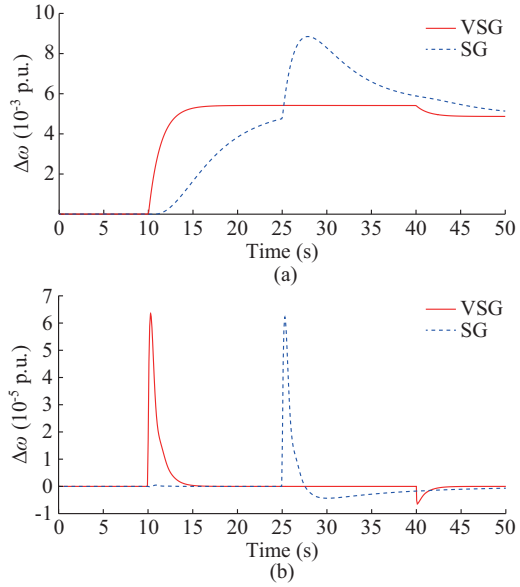

Fig. 8. Variations in frequency of VSG and SG after disturbances. (a) Basic VSG control method. (b) MPC-based VSG control method.

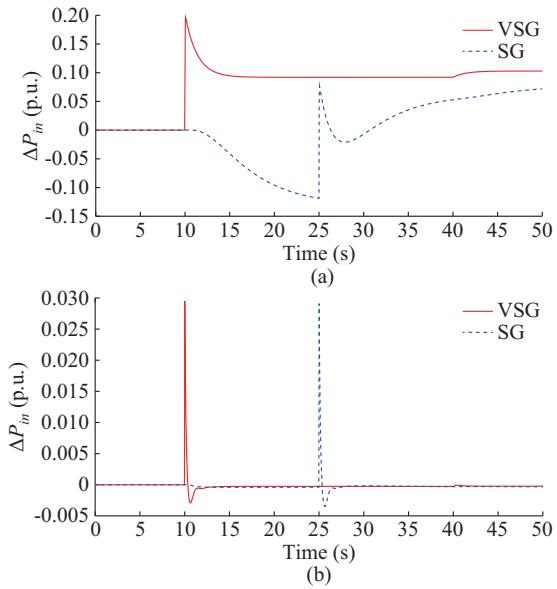

Fig. 9. Variations in input active power of VSG and SG after disturbances. (a) Basic VSG control method. (b) MPC-based VSG control method.

The input power of VSG is increased at $t=10$ s owing to the increase in the reference active power of VSG. It can be observed that the frequencies of both VSG and SG deviate significantly from their original operating points. At $t=25$ s, the frequency of SG increases with an increase in the reference active power of SG. The slight drop in frequencies of both VSG and SG at $t=40$ s is due to the increase in the reference reactive power of VSG. With the basic VSG control method for islanded operation, the frequencies of VSG and SG are not restored after disturbances, and a large amount of overshoot occurs owing to the absence of a primary network. As a result, the basic VSG control method cannot provide robust frequency behavior in both transient and steady-state analyses. For example, at $t=10$ s, the frequency overshoot of VSG reaches 0.0054 p.u. and the steady-state error remains at 0.0049 p.u., highlighting its poor regulation performance. Hence, an improved control method is required.

B. MPC-based VSG Control Method

The MPC is added to VSG control to enhance the transient behavior and minimize the steady-state error of the frequency response. After detecting frequency changes, MPC attempts to calculate the required reference active and reactive power of VSG and the reference active power change of SG. The outputs of MPC, which are the optimized signals of the active and reactive power, are set as the input signals of the VSG and SG at each sampling time.

The dynamic responses associated with the variations in frequency and input active power of VSG and SG with the MPC-based VSG control method after disturbances are shown in Figs. 8(b) and 9(b), respectively. With the changes in reference active power of VSG at $t=10$ s, the frequency response experiences an overshoot during the disturbance. However, there are two main differences between MPC-based and basic VSG control methods: ① the amount of frequency overshoot is significantly reduced with the MPC-based VSG control method, and ② the frequency response with the MPC-based VSG control method demonstrates robust stable behavior by returning to the original operating point shortly after the disturbance (frequency restoration).

Specifically, at $t=10$ s, the frequency overshoot of the VSG is only 6.32×10^{-5} p.u., and the steady-state error is zero, validating the improved transient and steady-state performance. The same behavior is observed for the changes in reference active power of SG at $t=25$ s.

Figure 10 illustrates the frequency responses of VSG and SG with different control methods under the predefined disturbances (as outlined in Table I) and a short-circuit fault. Specifically, the short-circuit fault is applied at node b from $t=30$ s to $t=30.2$ s to assess the robustness and stability of the MPC-based VSG control method.

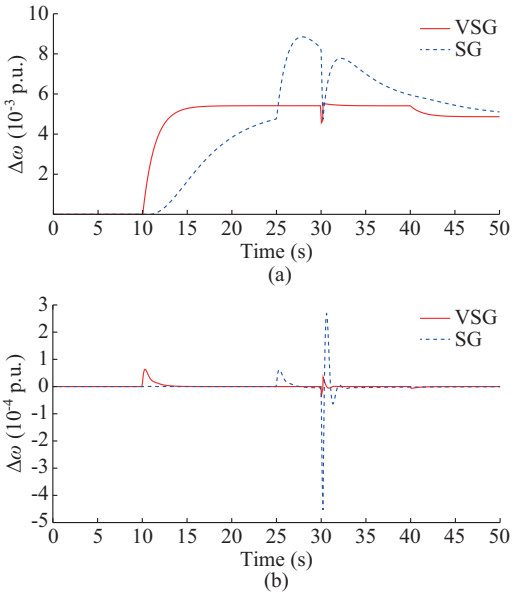

Fig. 10. Frequency response of VSG and SG with different control methods under predefined disturbances and a short-circuit fault. (a) Basic VSG control method. (b) MPC-based VSG control method.

Figure 10 clearly demonstrates that the MPC-based VSG control method maintains better frequency stability and faster recovery speed than the basic one, even under severe fault conditions. This highlights the effectiveness of the MPC-based VSG control method in handling transient events and maintaining system stability.

To verify the impact of the VSG parameters on the frequency response, the variations in VSG frequency with basic and MPC-based VSG control methods under different inertia constants and damping coefficients are shown in Figs. 11 and 12, respectively.

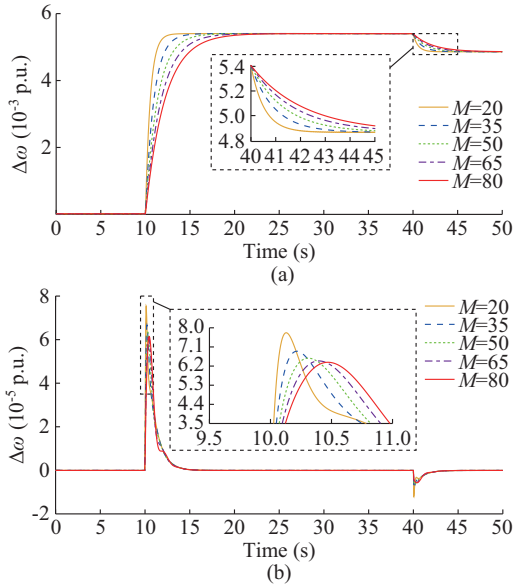

Fig. 11. Variations in VSG frequency with basic control method and MPC-based VSG control method under different inertia constants. (a) Basic control method. (b) MPC-based VSG control method.

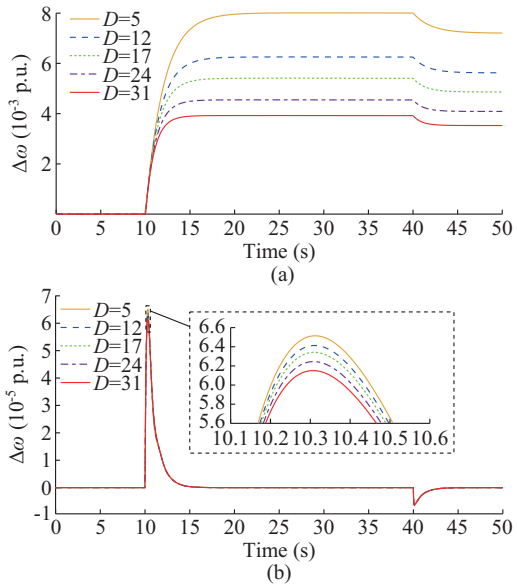

Fig. 12. Variations in VSG frequency with basic control method and MPC-based VSG control method under different damping coefficients. (a) Basic control method. (b) MPC-based VSG control method.

Although the frequency overshoot decreases by increasing the inertia constant of VSG, the system frequency shows more oscillatory behavior. In addition, higher damping coefficients result in lower frequency overshoots. With the MPC-based control method, compared with the basic one, the frequency changes are significantly reduced, and the controller is more robust to variations in the inertia constant and damping coefficient.

C. Communication Delay Compensation

As mentioned in Section III, the communication delay is a serious issue that must be addressed during the frequency control process when transferring data from the control center to the system. This delay causes frequency oscillations and instability issues. To overcome this problem, the ADC is obtained through system modeling. The ADC must compensate for communication delays without disrupting the functionality of system. To validate the ADC, the paralleled VSG-SG system is simulated while considering the communication delay in this scenario.

ADC is added to the MPC-based VSG control method, taking into account the 0.2 s communication delay. Figures 13 and 14 show a comparison of the variations in VSG and SG frequencies, respectively, with basic VSG control method, MPC-based VSG control method, and MPC-based VSG control method+ADC (which is referred to as the proposed control for simplicity).

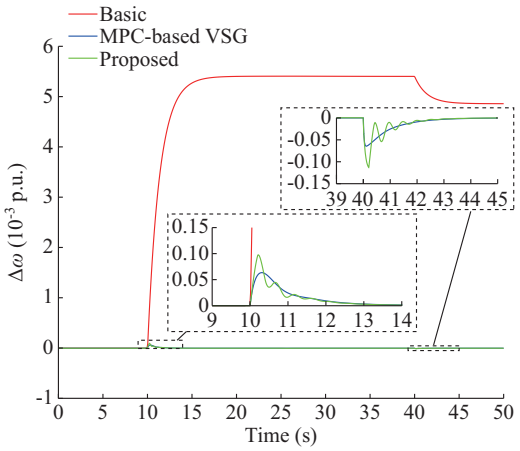

Fig. 13. Variations in VSG frequency with different control methods.

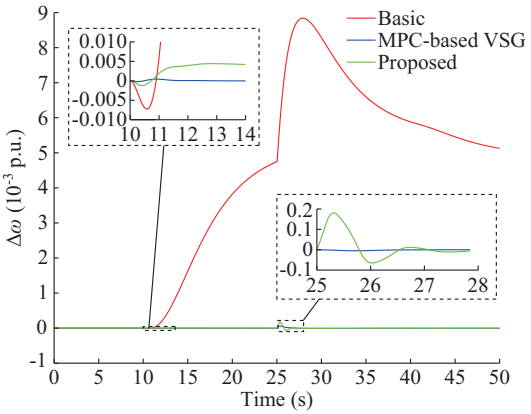

Fig. 14. Variations in SG frequency with different control methods.

With the proposed control, in the presence of ADC, the variations in VSG frequency are much less than those with the basic VSG control and are also restored under disturbances. However, it can be demonstrated that the frequency variations in both the VSG and SG with the proposed control show some oscillatory transient behaviors owing to the communication delay. However, the robust performance is guaranteed even with the presence of communication delay using the MPC method.

As mentioned previously, the delays depend on various factors such as the type of communication medium. To evaluate the robustness of the proposed control, the paralleled VSG-SG system is simulated considering different communication delays: $\tau_d = 200$ ms, $\tau_d = 400$ ms, and $\tau_d = 600$ ms.

The variations in VSG and SG frequencies are shown in Figs. 15 and 16, respectively, considering different communication delays.

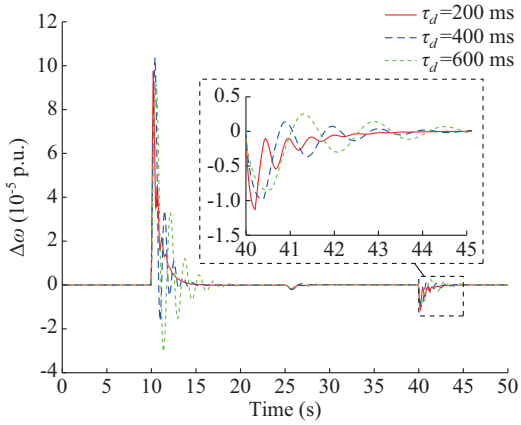

Fig. 15. Variation in VSG frequency considering different communication delays.

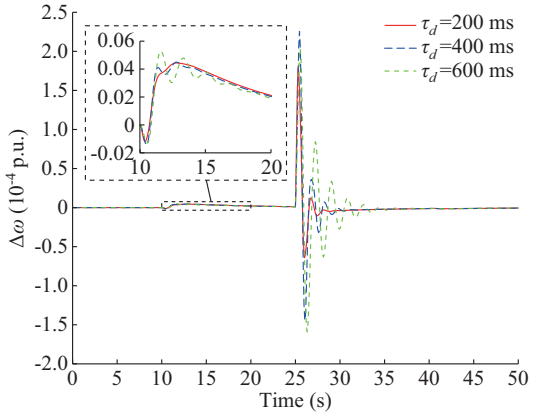

Fig. 16. Variations in SG frequency considering different communication delays.

The results indicate that the increased communication delay deteriorates the oscillatory response of the system frequency with increased solving time. This is also true for variations in the input active power of VSG and SG, as shown in Figs. 17 and 18, respectively. It can be observed that an increase in the amount of delay endangers the system stability.

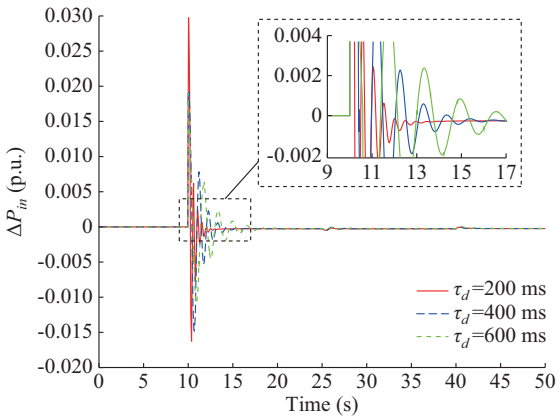

Fig. 17. Variations in input active power of VSG considering different communication delays.

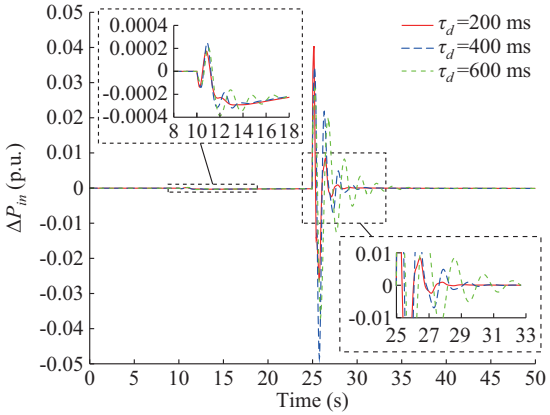

Fig. 18. Variations in input active power of SG considering different communication delays.

V. Conclusion

This paper develops a comprehensive dynamic model of an islanded system for the paralleled operation of VSG and SG supplying an RL load. Because the system is not connected to the power grid, the frequency variations are not restored. To resolve this problem, a central MPC-based VSG control method is applied to efficiently improve the system frequency. The performance of the proposed control is evaluated in different scenarios, and it is shown that using the proposed control, some of the response characteristics such as overshoot, steady-state error, and rate of change of frequency are significantly enhanced. Consequently, the frequencies are restored, and the system stability is improved. In addition, the power oscillations are reduced with the proposed control applied to the frequency control, allowing for an energy storage system with a lower capacity and consequent reduction in operational costs. Moreover, the effects of the damping coefficient and inertia constant are investigated in terms of frequency behavior. An ADC is employed to compensate for the communication delay, which results in some time required to send commands from the control center to the system. The participation of the ADC in MPC eliminates communication delays and avoids system instability. The impact of changes in the communication delay on system performance is also considered in the simulations. The results

validate the effectiveness and robustness of the proposed control. The frequency nadir and rate of change of the frequency are significantly enhanced, and the impacts of uncertainties and disturbances on the power system frequency decrease significantly.

The contributions of this paper are twofold. First, a robust MPC framework tailored for VSG-SG coordination in low-inertia systems is developed, and second, the delay compensation is integrated to preserve stability and performance in real-time applications.

From an engineering perspective, the proposed control is well-suited for practical deployment in microgrids and distributed energy systems, where maintaining frequency stability is a critical challenge. Its modular and scalable design allows for large-scale implementation, particularly in modern grids with increasing reliance on RESs. These findings provide a solid foundation for future work, including experimental validation and real-world implementation of hardware-in-the-loop (HIL) platforms and pilot microgrid projects. In practice, power overshoots may lead to high output currents, which can potentially trigger overcurrent protection mechanisms embedded in the VSG hardware. Although our simulation assumes ideal conditions without enforcing hardware current limits, designing a controller to constrain the power overshoot within acceptable bounds is important. This can be achieved by including current limiters or saturation blocks in the control loop or by incorporating current constraints directly into the MPC optimization. Future work will focus on the integration of these constraints to ensure protection coordination under transient conditions.

REFERENCES

[1] M. Toulabi, S. Bahrami, and A. M. Ranjbar, "Optimal supplementary frequency controller design using the wind farm frequency model and controller parameters stability region," *ISA Transactions*, vol. 74, pp. 175-184, Mar. 2018.

[2] A. Akbari, A. Alavi-Koosha, M. Moradi-Sepahvand *et al*., "An incentive mechanism for electric vehicles participation in security constrained unit commitment of renewable-integrated smart grids," *IEEE Transactions on Industrial Informatics*, vol. 20, no. 3, pp. 3824-3834, Sept. 2023.

[3] H. M. A. Ahmed, H. F. Sindi, M. A. Azzouz *et al*., "Optimal sizing and scheduling of mobile energy storage toward high penetration levels of renewable energy and fast charging stations," *IEEE Transactions on Energy Conversion*, vol. 37, no. 2, pp. 1075-1086, Jun. 2022.

[4] H. Aliamooei-Lakeh, S. Aliamooei-Lakeh, M. Toulabi *et al*., "Enhancement in robust performance of boost converter-based distributed generations utilizing active disturbance rejection controller," *IEEE Transactions on Automation Science and Engineering*, vol. 21, no. 4, pp. 6094-6108, Oct. 2024.

[5] C. Pradhan, C. N. Bhende, and A. K. Samanta, "Adaptive virtual inertia-based frequency regulation in wind power systems," *Renewable Energy*, vol. 115, pp. 558-574, Jan. 2018.

[6] M. Mahmoudnia, T. Amraee, and M. Toulabi, "Enhancing security and frequency control: integrating wind turbine participation in power electronics-controlled sustainable grids operation," *IEEE Transactions on Consumer Electronics*, vol. 71, no. 1, pp. 1647-1660, Oct. 2024.

[7] A. Ashouri-Zadeh, M. Toulabi, A. S. Dobakhshari *et al*., "Frequency stability improvement in wind-thermal dominated power grids," *IET Generation, Transmission & Distribution*, vol. 14, no. 4, pp. 619-627, Feb. 2020.

[8] Y. Hirase, K. Abe, K. Sugimoto *et al*., "A novel control approach for virtual synchronous generators to suppress frequency and voltage fluctuations in microgrids," *Applied Energy*, vol. 210, pp. 699-710, Jan. 2018.

[9] H. Bevrani, B. Francois, and T. Ise, *Microgrid Dynamics and Control*. Hoboken: John Wiley & Sons, 2017.

[10] M. Pourmohammad, M. Toulabi, and A. M. Ranjbar, "Application of state feedback controller to ensure robust D-stable operation of virtual synchronous generators," *IEEE Transactions on Energy Conversion*, vol. 36, no. 2, pp. 602-610, Jun. 2021.

[11] D. Ochoa and S. Martinez, "Frequency dependent strategy for mitigating wind power fluctuations of a doubly-fed induction generator wind turbine based on virtual inertia control and blade pitch angle regulation," *Renewable Energy*, vol. 128, pp. 108-124, Dec. 2018.

[12] K. M. Cheema, "A comprehensive review of virtual synchronous generator," *International Journal of Electrical Power & Energy Systems*, vol. 120, p. 106006, Sept. 2020.

[13] Y. Hirase, O. Noro, H. Nakagawa *et al*., "Decentralised and interlinkless power interchange among residences in microgrids using virtual synchronous generator control," *Applied Energy*, vol. 228, pp. 2437-2447, Oct. 2018.

[14] T. Kerdphol, M. Watanabe, K. Hongesombut *et al*., "Self-adaptive virtual inertia control-based fuzzy logic to improve frequency stability of microgrid with high renewable penetration," *IEEE Access*, vol. 7, pp. 76071-76083, Jun. 2019.

[15] M. Pourmohammad and M. Toulabi, "Designing a central MIMO state feedback controller for a microgrid with multi-parallel VSGs to damp active power oscillations," *International Journal of Electrical Power & Energy Systems*, vol. 133, p. 106984, Dec. 2021.

[16] K. Y. Yap, C. R. Sarimuthu, and J. M. Lim, "Virtual inertia-based inverters for mitigating frequency instability in grid-connected renewable energy system: a review," *Applied Sciences*, vol. 9, no. 24, p. 5300, Dec. 2019.

[17] Q. Zhang, Y. Li, Z. Ding *et al*., "Self-adaptive secondary frequency regulation strategy of micro-grid with multiple virtual synchronous generators," *IEEE Transactions on Industry Applications*, vol. 56, no. 5, pp. 6007-6018, Sept.-Oct. 2020.

[18] Y. Zhang, Q. Sun, J. Zhou *et al*., "Optimal frequency control for virtual synchronous generator based AC microgrids via adaptive dynamic programming," *IEEE Transactions on Smart Grid*, vol. 14, no. 1, pp. 4-16, Aug. 2022.

[19] P. Liu, Y. Bi, and C. Liu, "Data-based intelligent frequency control of VSG *via* adaptive virtual inertia emulation," *IEEE Systems Journal*, vol. 16, no. 3, pp. 3917-3926, Dec. 2021.

[20] Y. Wang and R. J. Wai, "Adaptive fuzzy-neural-network power decoupling strategy for virtual synchronous generator in micro-grid," *IEEE Transactions on Power Electronics*, vol. 37, no. 4, pp. 3878-3891, Apr. 2022.

[21] D. B. Rathnayake, S. P. Me, R. Razzaghi *et al*., "H_∞-based control design for grid-forming inverters with enhanced damping and virtual inertia," *IEEE Journal of Emerging and Selected Topics in Power Electronics*, vol. 11, no. 2, pp. 2311-2325, Nov. 2022.

[22] K. Mentesidi, R. Garde, M. Aguado *et al*., "Implementation of a fuzzy logic controller for virtual inertia emulation," in *Proceedings of 2015 International Symposium on Smart Electric Distribution Systems and Technologies*, Vienna, Austria, Sept. 2015, pp. 606-611.

[23] L. Lyu, X. Wang, L. Zhang *et al*., "Fuzzy control based virtual synchronous generator for self-adaptative control in hybrid microgrid," *Energy Reports*, vol. 8, pp. 12092-12104, Nov. 2022.

[24] A. Fathi, Q. Shafiee, and H. Bevrani, "Robust frequency control of microgrids using an extended virtual synchronous generator," *IEEE Transactions on Power Systems*, vol. 33, no. 6, pp. 6289-6297, Nov. 2018.

[25] T. Liu, A. Chen, F. Gao *et al*., "Double-loop control strategy with cascaded model predictive control to improve frequency regulation for islanded microgrids," *IEEE Transactions on Smart Grid*, vol. 13, no. 5, pp. 3954-3967, Sept. 2022.

[26] B. Long, X. Li, J. Rodriguez *et al*., "Frequency stability enhancement of an islanded microgrid: a fractional-order virtual synchronous generator," *International Journal of Electrical Power & Energy Systems*, vol. 147, p. 108896, May 2023.

[27] B. Long, Y. Liao, K. Chong *et al*., "MPC-controlled virtual synchronous generator to enhance frequency and voltage dynamic performance in islanded microgrids," *IEEE Transactions on Smart Grid*, vol. 12, no. 2, pp. 953-964, Mar. 2021.

[28] B. Naduvathuparambil, M. C. Valenti, and A. Feliachi, "Communication delays in wide area measurement systems" in *Proceedings of Proceedings of the Thirty-Fourth Southeastern Symposium on System Theory*, Huntsville, USA, Nov. 2002, pp. 118-122.

[29] H. Zhang, D. Li, H. Liu *et al*., "Comparison of low frequency oscillation characteristic differences between VSG and SG," in *Proceedings of 2020 IEEE Sustainable Power and Energy Conference*, Chengdu,

China, Jul. 2020, pp. 668-673.
[30] J. Alipoor, Y. Miura, and T. Ise, "Power system stabilization using virtual synchronous generator with alternating moment of inertia," *IEEE Journal of Emerging and Selected Topics in Power Electronics*, vol. 3, no. 2, pp. 451-458, Jun. 2015.
[31] P. S. Kundur and O. P. Malik, *Power System Stability and Control*. New York: McGraw-Hill Education, 2022.
[32] M. Eremia and M. Shahidehpour, *Handbook of Electrical Power System Dynamics: Modeling, Stability, and Control*. Hoboken: Wiley-IEEE Press, 2013.
[33] C. Bordons, F. Garcia-Torres, and M. A. Ridao, *Model Predictive Control of Microgrids*. New York: Springer, 2020.

Mohammadreza Najafi received the B.Sc. degree in electrical engineering from Ferdowsi University of Mashhad, Mashhad, Iran, in 2020, and the M. Sc. degree in power system from K. N. Toosi University of Technology, Tehran, Iran, in 2024. His research interests include power system frequency stability and control.

Hossein Aliamooei-Lakeh received the B. Sc. degree in mechanical engineering from K. N. Toosi University of Technology, Tehran, Iran, in 2022. His research interests include microgrid, renewable energy, optimization, and load frequency control.

Hessam Kazari received the B. Sc., M. Sc., and Ph. D. degrees in electrical engineering from Sharif University of Technology, Tehran, Iran, in 2009, 2011, and 2019, respectively. Currently, he is working as Assistant Professor in the Department of Electrical Engineering at Iran University of Science and Technology, Tehran, Iran. His research interests include power system operation, energy storage system, and renewable energy resource.

Mohammadreza Toulabi received the B. Sc., M. Sc., and Ph. D. degrees in electrical engineering (power systems) from Sharif University of Technology, Tehran, Iran, in 2010, 2012, and 2018, respectively. He is currently an Assistant Professor in the Department of Electrical Engineering at K. N. Toosi University of Technology, Tehran, Iran. His research interests include power system dynamics, power system operation and control, wind energy conversion system, renewable energy integration, and control system.